

## Article

# A Best-Path Approach to the Design of a Hybrid Space–Ground Quantum Network with Dynamic Constraints

David L. Bakker , Yannick Jong, Bob P. F. Dirks  and Gustavo C. Amaral \* 

The Netherlands Organization for Applied Scientific Research (TNO), Stieltjesweg 1, 2628 CK Delft, The Netherlands; david.bakker@tno.nl (D.L.B.); yannick.jong@tno.nl (Y.J.); bob.dirks@tno.nl (B.P.F.D.)

\* Correspondence: gustavo.castrodoamaral@tno.nl

**Abstract:** The design and operation of quantum networks are both decisive in the current push towards a global quantum internet. Although space-enabled quantum connectivity has already been identified as a beneficial candidate for long-range quantum channels for over two decades, the architecture of a hybrid space–ground network is still a work in progress. Here, we propose an analysis of such a network based on a best-path approach, where either fiber- or satellite-based elementary links can be concatenated to form a repeater chain. The network consisting of quantum information processing nodes, equipped with both ground and space connections, is mapped into a graph structure, where edge weights represent the achievable secret key rates, chosen as the figure of merit for the network analysis. A weight minimization algorithm allows for identifying the best path dynamically, i.e., as the weather conditions, stray light radiance, and satellite orbital position change. From the results, we conclude that satellite links will play a significant role in the future large-scale quantum internet, in particular when node distances exceed 500 km, and both a constellation of satellites—spanning 20 or more satellites—and significant advances in filtering technology are required to achieve continuous coverage.

**Keywords:** quantum communications; quantum internet; quantum repeater architectures; satellite optical communications; best-path estimation



**Citation:** Bakker, D.L.; Jong, Y.; Dirks, B.P.F.; Amaral, G.C. A Best-Path Approach to the Design of a Hybrid Space–Ground Quantum Network with Dynamic Constraints. *Photonics* **2024**, *11*, 268. <https://doi.org/10.3390/photonics11030268>

Received: 14 February 2024

Revised: 6 March 2024

Accepted: 12 March 2024

Published: 18 March 2024



**Copyright:** © 2023 by the authors. Licensee MDPI, Basel, Switzerland. This article is an open access article distributed under the terms and conditions of the Creative Commons Attribution (CC BY) license (<https://creativecommons.org/licenses/by/4.0/>).

## 1. Introduction

The future quantum internet will enable connectivity between quantum information processing (QIP) nodes through the continuous distribution of entanglement [1,2]. In stricter terms, this translates into high-rate long-distance transmission of multi-partite quantum states exhibiting high fidelity with respect to maximally entangled states of the same dimension—for the simpler case of two QIP nodes, the fidelity with respect to a Bell state [3]. In general, the requirements of high rate and high fidelity play opposing roles as far as entanglement generation processes are concerned, as exemplified by the widely used sources of entangled photon pairs based on non-linear media [4]: by increasing the pump power, more photon pairs are generated at the expense of multi-photon pair states that diminish the overall state fidelity. On top of that, preservation of both rate and fidelity after long-distance transmission represents an even bigger challenge, albeit one that many research groups around the world are willing to undertake [5–7]. The core idea is to break down the long distances into smaller stretches, called elementary links, where entanglement can be efficiently distributed in a heralded manner, such that quantum memories preserve the successful results. A chain of elementary links acts as a quantum repeater, where the intrinsic losses of the channel are mitigated by the rounds of entanglement swapping preserved by the quantum memories [8]. Finally, the entanglement is distributed to the end nodes [9], thereby achieving a network of interconnected quantum processors. Although some speculate that the so-called “killer application” of a quantum internet has not yet been identified, the prospects of secure communication relying on quantum

key distribution and increased quantum processing power due to distributed quantum computing, both on a global scale, drive the progress and push for innovative solutions.

Satellite-based quantum communication opens the door to long-distance entanglement distribution links with a reduced number of elementary links in the quantum repeater chain. Apart from the tens of kilometers of atmosphere, light propagates through vacuum on its path towards (or from) the satellite, so the dominating loss term is the so-called free space path loss (FSPL), which scales quadratically with distance instead of exponentially, as the loss in an optical fiber [10]. In ground-based networks, quantum repeater nodes must be located at an accessible location and the fiber can rarely be installed in a straight line between two consecutive nodes, exemplified in metropolitan experiments [11,12]. The added benefit of independence concerning the topographical conditions of a certain node could further position satellites as an enabling quantum repeater node even for shorter distances. Furthermore, when a quantum internet that spans the entire globe is considered, the requirement of transoceanic links strongly favors the use of non-ground-based repeater nodes, achievable with space-based links. The expensive and complex endeavor of flying a space-qualified quantum payload on a satellite, coupled to the fact that current quantum memory platforms are not yet capable of supporting the long-distance links that make satellites beneficial, poses significant challenges for space-based quantum communications; this issue currently attracts a small number of early adopters: the Micius satellite figures as the pioneer quantum satellite mission [13], but it is not the only one [14]. Therefore, the main focus remains on ground-based quantum networks [12,15–17], and a shift in perspective requires both significant advances in the enabling technologies (sources of entangled photon pairs and quantum memories for light) and a clear definition of the benefits of a satellite-based link and the requirements such that these benefits can materialize [18–21].

Here, a contribution to the latter is put forth: an analysis of entanglement distribution rates between two arbitrary nodes in a quantum network that allows both ground- and satellite-based links. We start by breaking down the building blocks of a quantum repeater and rearranging them to fit a space segment all the while considering its practical constraints. This allows for us to write entanglement distribution rate equations for both satellite- and ground-based repeater channels, which are then mapped onto the weights of edges in a graph representing the network. A best-path algorithm is then used to evaluate the beneficial architecture. The analysis is capable of incorporating dynamic conditions of the satellite link, such as the weather, stray light and the satellite orbit, for which realistic data are employed. We show that satellites present significant advantages for longer distance links, as expected. Also, note that significant effort towards modeling and analyzing the achievable entanglement distribution rates in a practical quantum network has been made [22–25]. The present work is complementary, allowing for quick and broad analysis of practical quantum repeater architectures. The paper discusses the thresholds of satellite-based quantum communications, on the identified limits of the analysis as well as of the current technology, with conclusions on the potential avenues towards improvements.

## 2. Quantum Repeaters: Ground and Space Architectures

A quantum repeater leverages the multimodality (temporal, spectral, etc.) enabled by both the quantum memory and the heralded swapping of entanglement to decouple the individual probabilities of success within a so-called elementary link; it also beats the bounds of direct transmission [26]. Although different choices of protocol, encoding, platform, and wavelengths exist [27], the unavoidable functional blocks of a quantum repeater can be narrowed down to four: sources of entanglement, quantum memories, Bell State Measurement units, and quantum channels. The requirements on the sources are such that entanglement is generated at the best compromise between high rate and high fidelity, in as many multiplexed modes as possible, and with an optical interface so that optical photons can carry the quantum information with minimum attenuation and decoherence over the quantum channels. The quantum memories come in many flavours,

and it is common for a single platform to implement both memory and source in the same physical system [5,7,28]. Due to the latter not being the general case [6], the functional blocks are split. The memory is expected to store a quantum state in a large number of modes with high efficiency. The Bell State Measurement (BSM) unit maps the joint state of two non-interacting photons on the base of maximally entangled bipartite states and is at the core of the entanglement swapping protocol [29]. It is expected to efficiently produce projection measurement results that can be classically conveyed to the quantum memories to swap entanglement in a heralded fashion [30]. Here, efficiencies are understood as the probability that the functional block performs as expected. For the source, this means the probability of successfully emitting a single pair of entangled photons for a given attempt (compared to the probability of emitting zero or two or more pairs). An attempt is abstracted as a discrete event associated to a global clock, and the chosen encoding basis of the photonic qubits is also assumed not to alter the efficiency of the source. For the quantum memory, it means the probability of successfully storing and retrieving a photon from an entangled pair without disturbing its quantum state, i.e., the fidelity of storage in the memory, is independent from its efficiency. In case of the BSM, it means the probability of successfully mapping and detecting the joint photon state. By defining and abstracting efficiencies in such a way, they can be combined to yield a total efficiency of the quantum repeater.

Based solely on the natural disposition of the functional blocks within an elementary link [26,27,30], with source and memory on either side with a centralized BSM, it would be natural to assign the latter to the satellite. This way, two ground stations, each equipped with a source and a memory, would beam photons up to the satellite. The successful measurement results would be transmitted down to the ground stations, leaving the states stored in the memory in a joint entangled state. For a ground-based architecture, this configuration is extremely attractive, since the direction of propagation of the photonic qubits is irrelevant. However, the thin layer of atmosphere in the ground-to-satellite path close to the ground breaks the transmission direction symmetry for the space segment, as opposed to the fiber-based ground segment. The configuration in which the satellite receives a beam from a ground station is usually referred to as the uplink as opposed to the downlink, where the satellite sends beams to the ground stations. In the uplink, the beam experiences the effect of atmosphere at the first few kilometers of propagation, so the slightest angular deviation introduced there is translated into a significant beam spot displacement at the satellite, after hundreds of kilometers of propagation. On the other hand, the downlink does not suffer from the same problem simply because the beam only interacts with the atmosphere at the very end of the propagation path. Differences in total loss between the two configurations, depending on the atmospheric turbulence, vary between 10 and 100 times [31]. Therefore, the downlink configuration, i.e., photonic qubits transmitted from the satellite to the ground stations, is chosen as a baseline in this work.

Downlink configuration restricts the design of a quantum repeater's space segment containing a satellite since the source, rather than the BSM, is at the center point between the two ground stations. Placing the source on the satellite meets practical constraints, since these have been demonstrated to operate in-orbit [13,14], but relays all the complexity to the ground stations. Due to the probabilistic nature of entanglement distribution over lossy channels, successful rounds must be heralded by a classical signal coming from a BSM-like unit so that the quantum memories can hold on to those specific modes. While proposals such as [32] combine the memories and the BSM heralding protocol into a single system, the functional blocks can be easily kept separated, in which case a source and a BSM must be included in both ground stations. In this final configuration, the satellite beams photon pairs down to earth, and the pairs reach two ground stations. There, photons coming from space meet a photon generated on the ground in a BSM whose pair is stored in the quantum memory. Based on the simultaneous heralding event of both ground-based BSMs, the states in the quantum memories are left in an entangled state following entanglement swapping. The block diagram representation of both space and ground repeater segments introduced

so far is presented in Figure 1. Note that these are not the only possible architectures, but they offer a practical short- to mid-term architecture aside from intuitive functional roles of each block.

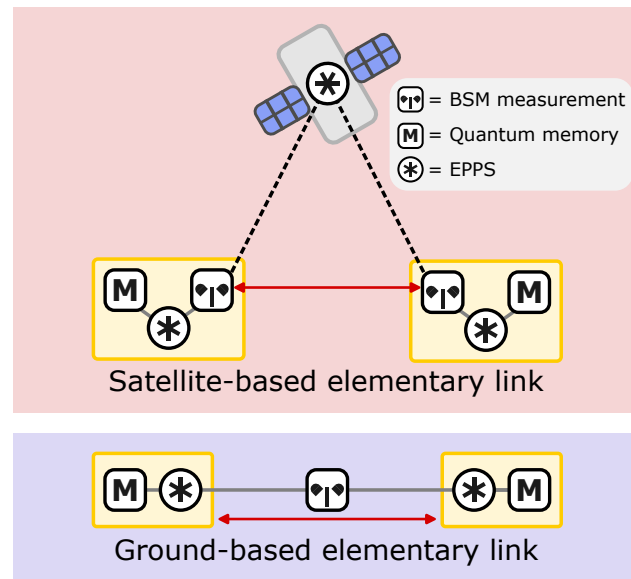


**Figure 1.** Basic space (top) and ground (bottom) segments of a quantum repeater. Dotted black lines represent free-space optics quantum channels, solid grey lines represent fiber optics quantum channels, and solid red arrows denote classical communication rounds. EPPS stands for Entangled Photon Pair Source.

The functional block description of quantum memory, source of entanglement, BSM, and quantum channel, equipped with efficiencies and fidelities, provides a powerful framework to analyze the overall efficiency of a given concatenation of space and ground segments with rounds of entanglement swapping: a so-called automated repeater chain (ARC) [27,33]. The ARC is assumed to perform subsequent attempts of entanglement distribution over each segment at a fixed rate  $R$ , which has the role, in a bipartite entanglement distribution scheme as considered here, of translating efficiencies into probabilities, and those into an average number of Bell pairs available at the end nodes. By enforcing minimum decoherence processes as the photonic qubits propagate through the quantum channels, negligible dark counts on the BSM detectors, and storage times long enough to ensure that the heralding signals reach the quantum memories in a timely manner (before the quantum states are lost), the performance of an ARC can be narrowed down to its achievable rate of entanglement distributed towards its end nodes. One can start by assigning efficiencies  $\eta_S$ ,  $\eta_M$ ,  $\eta_B$ , and  $\eta_{ch}(\ell_A)$ ,  $\eta_{ch}(\ell_B)$  to source, memory, BSM, and channels, respectively. Here,  $\ell_{A,B}$  denotes the optical path distance between the center point of an elementary link and either one of its nodes. It is worth noting that the efficiency of the channel is a function of its distance, which takes on a quadratic or exponential scaling in case of space or ground segments. Furthermore, the term ground segment is used to refer to a fiber connection. Ground-to-ground free-space channels are also an option, especially for the last mile to connect locations without a direct fiber link. However, their range is limited, typically several kilometers in urban areas [34]. Since they do not provide a significant benefit over optical fibers, ground segments are safely assumed to be represented solely by the latter.

To arrive at the ground-based elementary link (EL) rate equation [27], one starts from the success probability of a single attempt, which, for a ground segment, is simply the  $\eta_S^2 \eta_B \eta_{ch:g}(\ell_A) \eta_{ch:g}(\ell_B)$  product. This value can be subtracted from unity to represent the probability of no success, which, when taken to the power of the available number of multiplexing modes ( $\Gamma$ ) available, represents the probability that no modes were successful

within a given attempt. Subtracting the latter term from unity and multiplying it by  $\eta_M^2$  equates to the probability of at least one mode being successfully swapped and stored into the quantum memories, the result of which is summarized in the expressions below:

$$P_{gnd}^{EL}(\ell_A, \ell_B) = \left(1 - \left[1 - \eta_S^2 \eta_B \eta_{ch:g}(\ell_A) \eta_{ch:g}(\ell_B)\right]^\Gamma\right) \eta_M^2, \tag{1}$$

$$\eta_{ch:g}(\ell) \propto e^{-\alpha \ell}. \tag{2}$$

The steps towards the space-based EL rate equation are the same, although the different configuration of the functional blocks must be accounted for as well as the difference in channel losses, as expressed below:

$$P_{spc}^{EL}(\ell_A, \ell_B) = \left(1 - \left[1 - \eta_S^3 \eta_B^2 \eta_{ch:s}(\ell_A) \eta_{ch:s}(\ell_B)\right]^\Gamma\right) \eta_M^2, \tag{3}$$

$$\eta_{ch:s}(\ell) \propto (\theta \ell)^{-2}. \tag{4}$$

Factors  $\alpha$  in Equation (2) and  $\theta$  in Equation (4) denote the fiber attenuation coefficient and half-angle divergence of the free-space optical beam, respectively. It should also be noted that, although the distances  $\ell_{A,B}$  of a ground segment correspond directly to distances between the nodes and the central point, those for space consider the distances towards the satellite. An ARC is formed through the concatenation of its  $n$  segments through  $n - 1$  steps of successful entanglement swapping, leading to a final probability of entanglement distribution of the following form:

$$P^{ARC} = \eta_B^{(n-1)} \prod_{i=1}^g P_{gnd}^{EL}(\ell_{Ai}, \ell_{Bi}) \prod_{k=1}^s P_{spc}^{EL}(\ell_{Ak}, \ell_{Bk}), \tag{5}$$

where  $g + s = n$ .

It is interesting to note that the potential benefit of the space segment relies heavily on whether the quadratic loss scaling can beat the exponential scaling of the fiber and the increased complexity of the ground station hardware. This point is made more stringent due to the fact that the distance covered by a ground segment can be approximated by the distance between the two ground stations, while for a space segment, the distance depends on the altitude of the satellite. In other words, two ground stations separated by 100 km can be connected by 100 km of optical fibers, but the fact that the satellite is hovering at a  $\geq 500$  km altitude causes the optical path for the space segment to be much longer. The expression of Equation (5), however, tells only part of the story: as previously discussed, entanglement distribution in a quantum network relies on the transmission of entangled particles with high rate and high fidelity. The secret key rate (SKR) combines both requirement aspects of the ARCs into a single meaningful parameter [35] and is widely used as a figure of merit for the quality of quantum networks, although new benchmarking procedures have been proposed, e.g., [36]. The SKR allows for the evaluation of relevant practical issues, the most pressing for satellite quantum channels being the impact of stray light.

Stray light refers to unfiltered photons that are mixed in the path of the photonic qubits transmitted by the satellite. These reduce the quantum information capacity of the link. Although any decoherence process during transmission through the channel is neglected in the present analysis, stray light has a severe impact on the results of the BSM units, especially during the day, when solar radiance is maximum. In order to evaluate the impact of the unwanted photons on the overall fidelity of the states distributed over the ARCs, a decoherence channel model is assumed. The states produced by the source are considered to be Werner states (noisy EPR pairs) [37] with an associated density matrix of the following form:

$$\rho_S = \mathcal{W}_S |\phi^+\rangle \langle \phi^+| + \frac{1-\mathcal{W}_S}{4} \mathbb{I}_4, \tag{6}$$

where  $|\phi^+\rangle$  is a maximally entangled Bell state,  $\mathcal{W}_S$  is the Werner parameter of the source associated with its fidelity with respect to  $|\phi^+\rangle$ , and  $\mathbb{I}$  is a  $4 \times 4$  identity matrix. The final Werner parameter of the states available on the ground stations can be estimated by concatenating the Werner parameters of each functional block, which are assumed to be fixed except for the BSM.

The Werner parameter of the swapped states due to the action of the BSM can be estimated from the Coincidence-to-Accidental Ratio (CAR), which approximates the signal-to-noise ratio (SNR) achievable at the BSM. In the regime of low decoherence introduced by the quantum channel, the CAR provides an upper bound of the fringe visibility extracted from the coincidence measurements performed on joint state  $\rho^{EL}$  delivered by the ARC segment. The visibility, in turn, is directly associated to the Werner parameter of the link, where the term introduced by the BSM,

$$\mathcal{W}_B \approx \frac{CAR - 1}{CAR + 1}, \tag{7}$$

is dominant. With this expression, one can connect the stray light radiance impinging on the BSM detectors to the overall entanglement quality generated in an ARC segment. First, the stray photon rate can be derived given solar radiance (which can be approximated to have a black body radiation profile  $I_{stray}$ ); the receiver telescope parameters of the aperture area ( $A_{RX}$ ) and the solid angle ( $\Omega$ ); the photonic qubit bandwidth ( $B_\lambda$ ); and the operational wavelength ( $\lambda$ ):

$$R_{stray} = I_{stray} \Omega A_{RX} B_\lambda / \left( \frac{hc}{\lambda} \right), \tag{8}$$

where  $h$  is Planck’s constant and  $c$  is the speed of light. Rate  $R_{stray}$  is then translated into the term  $p_{stray}$  (the probability of measuring a stray photon within a time window of the detectors), with the assumption that the stray detection events are uncorrelated and thus homogeneously distributed over time. Therefore,  $p_{stray} = R_{stray} \cdot \delta t$ , where time resolution  $\delta t$ —limited by the detector’s jitter or response time—is imposed. Finally, the photonic qubits are expected at a well-defined time window,  $w_{det}$ ; therefore,

$$CAR = \frac{\int_{w_{det}} P_{gnd/spc}^{EL}(\ell_A, \ell_B) dt}{\int_{w_{det}} (p_{stray})^2 dt}. \tag{9}$$

In Equation (9), the term  $P_{gnd/spc}^{EL}$  is not squared since it already presumes pairs of photons arriving at the BSM. From it, the estimated entanglement quality delivered by a given ARC segment (directly proportional to the overall Werner parameter  $\mathcal{W}^{EL}$ ) is directly calculated from the multiplication of  $\mathcal{W}_B$  and the remaining individual Werner parameters of the other functional blocks of the elementary links ( $\mathcal{W}_S, \mathcal{W}_M$ , for source and memory, respectively). Relevant for the SKR is the quantum bit error rate (QBER), approximated as  $\frac{1-\mathcal{W}^{EL}}{2}$  [38], which can be used to calculate the entropy per distributed entangled pair over the elementary link:

$$S_q^{EL} = \max(0, 1 - (1 + \kappa)\mathcal{H}(QBER)), \tag{10}$$

where  $\kappa$  is a constant representing the inefficiency of the classical steps of the quantum key distribution protocol, and  $\mathcal{H}$  is the Shannon entropy function. Note that the SKR, calculated as product

$$SKR^{EL} = R S_q^{EL} P_{gnd/spc}^{EL}, \tag{11}$$

is heavily influenced by the entanglement generation probability of the elementary link, since it also impacts  $\mathcal{W}_B$ —as indicated in Equation (9)—making it the most significant term to optimize. This is relevant for the best-path estimation results of Section 3, since the SKR can only be computed at the end nodes at the edges of an ARC, while the optimization takes into account each individual segment.

### Modeling Free-Space Optical Channels

In the space segment, a satellite is the connecting point between two ground stations (A and B) and the entanglement generation probability depends on channel efficiencies  $\eta_{ch:s}(\ell_A)$  and  $\eta_{ch:s}(\ell_B)$ . Since the orbit of the satellite determines its position at any given point in time and the ground stations are static, these two terms may differ greatly. Evaluating  $\eta_{ch:s}(\ell_{A,B})$  follows from the identification of its four major contributing factors: the geometrical losses due to the beam divergence and limited receiver telescope dimensions,  $\eta_{fsl}$ ; the pointing losses due to vibrations, atmospheric turbulence and relative movement between transmitter and receiver stations,  $\eta_{pl}$ ; the effects of molecular and aerosol scattering in the atmosphere,  $\eta_{scat}$ ; and the coupling efficiency of the incoming free-space optical beam into a medium that allows for integration into the BSM unit, in general an optical fiber,  $\eta_{coup}$ . Given the individual contributions,  $\eta_{ch:s}(\ell_{A,B}) = \eta_{fsl}\eta_{pl}\eta_{scat}\eta_{coup}$ .

A detailed practical analysis of the first term can be found in [39]. It takes into account the sizes of both receiving and transmitting telescopes, the size of the beam after propagation with a certain divergence, clipping of the beam at the transmitting telescope, and obscurations in the telescopes. Assuming on-axis propagation and far-field approximation, optimal ratio  $\rho = a/\omega$  between the transmitter telescope’s diameter and beam waist can be derived [39]:

$$\rho \approx 1.12 - 1.30\gamma^2 + 2.12\gamma^4, \tag{12}$$

where  $\gamma$  is the obscuration ratio. The design ratio  $\rho$  allows one to write  $\eta_{fsl}$  given a few other design parameters as follows:

$$\eta_{fsl} = \frac{A_{TX}A_{RX}}{(\lambda\ell)^2} \frac{2}{\rho^2} \left[ e^{-\rho^2} - e^{-\gamma^2\rho^2} \right]^2, \tag{13}$$

where  $A_{TX}$  and  $A_{RX}$  are the aperture areas of the transmitting and receiving telescopes, respectively,  $\lambda$  is the operational wavelength, and  $\ell$  is the distance between the two telescopes. The beam waist  $\omega$ —defined by the choice of  $A_{TX}$  and Equation (12)—in turn defines the half-angle beam divergence,  $\theta$ , in radians. This is then used to compute  $\eta_{pl}$  through [40]

$$\eta_{pl} = \exp \left[ -2 \left( \frac{\theta_t}{\theta} \right)^2 \right], \tag{14}$$

where  $\theta_t$  is the half-angle pointing error, also in radians, which can be mitigated with an active pointing tracking system [13]. Differently from  $\eta_{fsl}$  and  $\eta_{pl}$ , the remaining term  $\eta_{scat}$  is only empirically modeled by the following expression [41]:

$$\eta_{scat} = T_c \exp \left( - \frac{\beta_0 \mathcal{H}_0}{\cos(Z)} \left[ 1 - \exp \left( - \frac{\ell \cos(Z)}{\mathcal{H}_0} \right) \right] \right), \tag{15}$$

where  $T_c$  is the cloud coverage factor,  $\beta_0$  is the extinction coefficient at sea level, which is a function of weather visibility  $V$  and operational wavelength  $\lambda$  [42],  $\mathcal{H}_0 = 6600$  m is the scale parameter, and  $Z$  is the Zenith angle between the ground station and the satellite. Note that, apart from  $\mathcal{H}_0$  and  $\lambda$ , all parameters of Equation (15) are conditional since they change depending on the conditions of the channel. That is also the case for  $\eta_{coup}$ , since the atmospheric conditions such as turbulence can impact its value differently depending on their intensity [41]. Assuming the ground stations are equipped not only with pointing tracking hardware to minimize the effects of Equation (14) but also with an adaptive optics system [43], the optimistic assumption of  $\eta_{coup} = 0.4$  is used for the remainder of the analysis.

### 3. Hybrid Ground/Space ARC Network Simulation

Once equipped with both ground and space segment architectures (Figure 1) and their associated performance metrics (Equations (5), (9) and (11)), one can attempt to optimize the entanglement generation rate between any two end nodes of an ARC embedded within a network. In order to do so, a framework with two major components is introduced: one is a potential future pan-European quantum network, with over 100 selected nodes representing major European cities distributed throughout the territory, which is presented in Figure 2; the second is a method to optimize the connections between any combination of end nodes in this network connected by an ARC. The latter is achieved by evaluating all the connections between the nodes in the network using the performance metrics introduced so far, associating them with edge weights of a graph, and searching for the best path.



**Figure 2.** Conceptual future pan-European quantum network dotted with Quantum Information Processing nodes (yellow triangles) connected via ARCs consisting of either ground or space segments (not depicted).

The evaluation process of the hybrid ARC network analyzes each unique combination of end-node pairs after a ground/space graph is built, hereby called a “hybrid” graph. First, a static graph is constructed, where all nodes are connected to each other via a fiber link. This graph is only constructed once, since it is assumed not to be changing over time. The second graph, based on space segment connections, is constructed for each time window considered in the evaluation (minute accuracy for practical purposes), where the weather conditions ( $V$  and  $T_c$ ) for each node of the network are selected from a historical database [44]. Figure 3 shows a flowchart of this process of constructing the hybrid graphs. For the simulation results, the weather conditions on the first of January 2024 are chosen without loss of generality. The time of the day is used to determine both the stray light radiance and the relative position of the satellite (in its polar orbit, at an altitude of 700 km) with respect to the ground stations. Since each node is assumed to be able to communicate with any other node directly (either via space or via ground segments), the two graphs are merged into a single hybrid graph. To that end, each node-to-node connection is evaluated individually based on its performance metric. Here, one can use the fact that the rate  $R$  of the ARC is assumed to be the same for ground and space segments to introduce the secret key probability,  $SKP = S_q^{EL} P_{gnd/spa}^{EL}$ . Since  $SKP \in [0, 1]$ , setting the edge weights as

$$w_E = -\log_{10}(SKP) \in [0, \infty) \tag{16}$$

ensures they are always positive and increase as the SKP (SKR) worsens. The segments with better performance are assigned to the edges of the hybrid graph: this allows for pruning and converging into a hybridized ground/space graph. Then, Dijkstra’s algorithm [45], which minimizes the path weight in a graph, can be used to estimate the best path between the chosen nodes, as pictorially presented in Figure 4. The choices of *ground-only*, *space-only*, or *hybrid*, as well as the final SKR, are recorded and the process moves on to the next round. The described procedure is not without its own limitations, starting from the fact that the weight estimated by Dijkstra’s algorithm at the end of each round does not represent the actual achievable SKR. The sum of the weights in a given path translates into the multiplication of the individual SKPs achieved by each segment of the path; although this would represent a meaningful value for the probability of entanglement generation (since probabilities can be multiplied), it does not necessarily equate the achievable SKR across a multi-segment path. In order to avoid edge cases that do not accurately represent the quality of an ARC, a tuple is assigned to each edge containing the values of SKP,  $S_q$ , and  $P_{gnd/spa}^{EL}(\ell_A, \ell_B)$ , where the latter term is used to tie-break which segment, ground or space, is chosen for the final graph. At the end of a round, the end-to-end SKR is calculated based on the total entanglement generation probability across the ARC (Equation (5)), and the total Werner parameter across the ARC.

$$\mathcal{W}^{ARC} = \prod_{i=1}^n \mathcal{W}_i^{EL}. \tag{17}$$

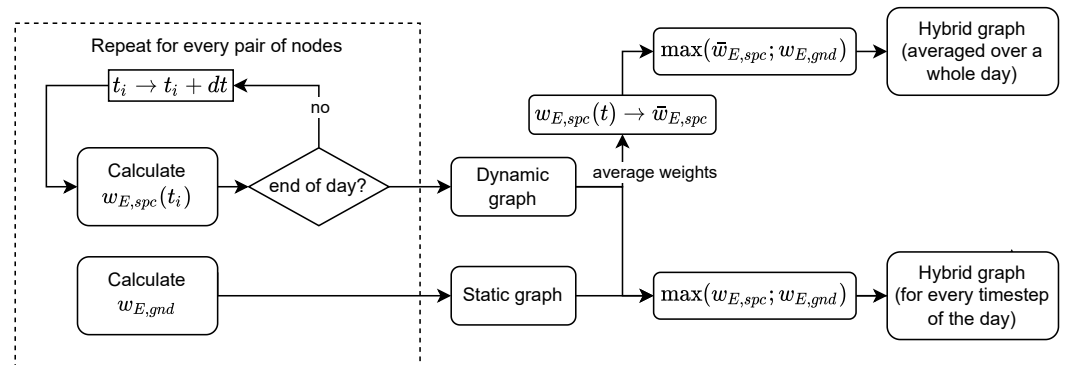


**Figure 3.** A flowchart showing the construction of the hybrid graph. Figure 5 uses the hybrid graph calculated with weights averaged over a day, while Figure 6 finds the best path for every time step in a graph built with non-averaged weights.

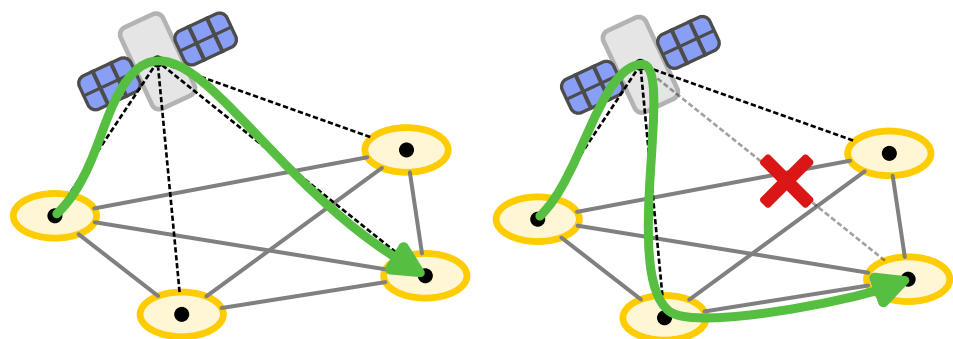


**Figure 4.** Pictorial representation of the best path estimation routine, where solid gray lines represent ground segments, dashed black lines represent space segments, nodes are represented by yellow circles, and the best path by green arrow. Left and right images represent situations where the same node selection produces different best path results (*space-only* or *hybrid*) due to dynamic constraints such as weather and stray light conditions or the relative position of the satellite.

Another constraint is associated with the computational efficiency of the procedure: although Dijkstra’s algorithm can converge quickly to the final solution, the step of building the final hybrid graph for each time window represents a bottleneck. By realizing that the fiber channel does not change significantly over time, as opposed to the free-space channel, the ground connections can be computed once and stored *a priori*. In doing so, one can notice that the number of ground-based elementary links that optimally connects two given nodes changes depending on the set of parameters, i.e., functional block efficiencies, Werner parameters, available modes, and total distance. Although assuming equal functional block parameters for ground and space segments and normalizing the efficiencies would allow more focus on the relative performance of the different architectures, ensuring that the results are obtained with realistic physical parameters is paramount. We set  $\eta_S = 0.25$ ,  $\eta_M = 0.75$ ,  $\mathcal{W}_S = \mathcal{W}_M = 0.99$ ,  $\Gamma = 300$ , keeping with the long-term ( $\sim 10\text{--}20$  years) expectations for potential functional block physical platforms [27]. According to the results presented in the next Section, the algorithm finds solutions in which the total distance between end nodes of the future European network shown in Figure 2 is divided into several concatenated elementary links of  $\sim 150$  km each in order to increase the overall rate.

#### 4. Results

We start by evaluating the network of Figure 2 assuming a fixed satellite positioned at 700 km above Zurich, such that the satellite is within a constant line of sight for most pairs of ground stations. We further assume night-time operation only. With this approach, the performance impact of the space segment is decoupled from issues associated to the management of the satellite. In Figure 5, the results of all unique combinations of end node pairs, evaluated according to the protocol described in Section 3, are presented in a scatter plot on the left hand side and color-coded, such that blue represents *ground-only*; black represents *space-only*; and red represents *hybrid*. There are cases where the key material that can be extracted from the link is null (*fail*), which do not appear in the scatter plot but are presented on the bottom right, where the total number for each individual channel choices are stratified. Note that the very choice of node placement introduces a bias in the average distance between QIPs, since metropolitan (shorter than 100 km) links are not included in the network of Figure 2. This choice follows from the immediate realization, clear from Equations (1) and (3), that satellites are unlikely to benefit short-range quantum networks. Therefore, comparison at short range distances is fruitless. Finally, Table 1 details the experimental parameters utilized in the simulation. Parameters not discussed are extracted from [27]. Solar radiation, cloud cover and visibility, and city coordinate data are scraped from an open source weather API [44].

**Table 1.** Table of parameters.

Parameter	Symbol	Value
Wavelength	$\lambda$	1550 nm
Source efficiency	$\eta_S$	0.25
Source fidelity	$\mathcal{F}_S$	0.99
Source rate	$R$	10 GHz
Memory efficiency	$\eta_M$	0.75
Memory fidelity	$\mathcal{F}_M$	0.99
Detector efficiency	$\eta_{DET}$	0.99
Detector jitter	$\delta t$	100 ps
Optical fiber attenuation	$\alpha$	0.146 dB/km
BSM efficiency	$\eta_B = 0.5 \times \eta_{DET}^2$	0.49005
Coupling efficiency	$\eta_{coup}$	0.4
Number of modes	$\Gamma$	300
Satellite obscuration	$\gamma_{sat}$	0
Satellite aperture	$d_{sat}$	0.3 m
Satellite pointing error	$\theta_t$	1.2 $\mu$ rad
Field-of-view OGS	FOV	50 $\mu$ rad
OGS aperture	$d_{ground}$	1.2 m

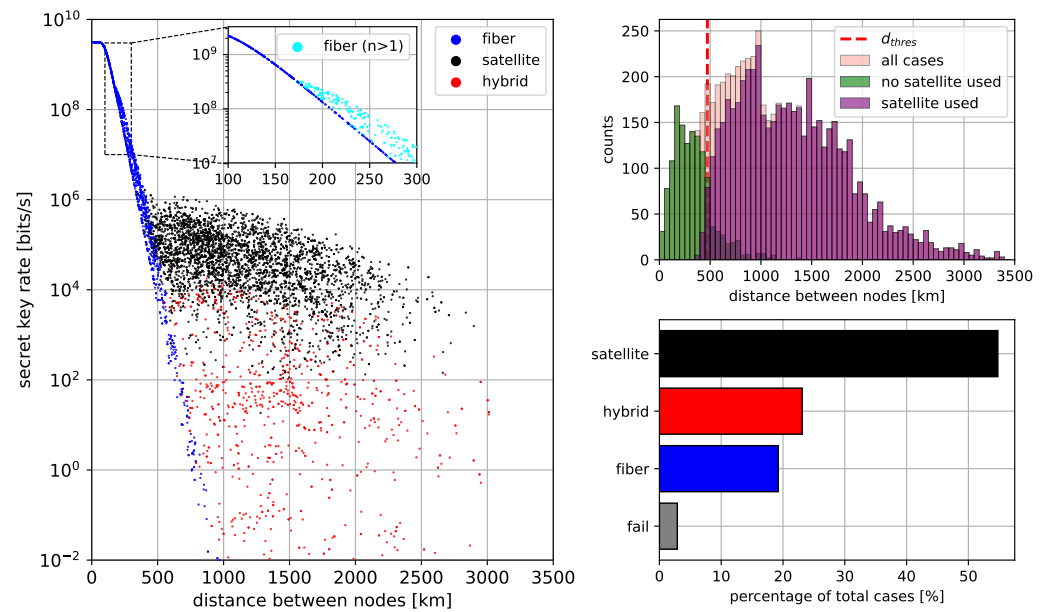


**Figure 5.** Channel performance for a hybrid ground/space European quantum network, as presented in Figure 2; the ARC rate  $R$  is set to 10 GHz. On the left, the color-coded scatter plot presents expected performance in terms of SKR versus node distance. In the excerpt, cases where the ground-based ARC decides on breaking the channel in more than one segment are highlighted in light blue, which happens mostly above 150 km, as expected. The performance results are agglutinated into the histogram presented on the top right, where the threshold that distinguishes the choice between ground and space is highlighted ( $d_{thres}$ ). Finally, the statistical distribution of the channel choices is presented on the bottom right corner, where the cases where key material is null (*fail*) are also presented.

The results depicted in Figure 5 indicate that, for the fixed satellite scenario, a clear distinction between different regimes appears. The first one is associated to the fact that, above the 150 km distance between end nodes, multiple ground segments are chosen instead of a single segment, as expected from Equation (1) and the parameters detailed in the previous Section. The second is the regime of ground preference versus space preference, which happens around 500 km. This result is further highlighted in the histogram on the top right corner. To determine the threshold distance  $d_{thres}$  of the regime switch, the histogram distributions of choices involving satellites and non-satellites are fitted to a log-normal distribution and the intersection point between the fit curves is calculated and represented by the segmented red vertical line. The fact that the results indicate a clear preference for space segments after a threshold of  $\sim 500$  km is noteworthy: although the preference is expected, identifying a practical regime switch can be significant. Also noteworthy is the large spread of black dots, associated to the dynamic nature of the weather conditions. Links with similar distance can have prominent differences in performance due to the weather. Finally, the expressive incidence of *hybrid* solutions indicates that the possibility to switch between space and ground segments is a valuable feature of the future quantum internet since, even for large distance links; the ARC benefits from having both available.

Moving on from the ideal case where the satellite and weather conditions are static requires taking into account the dynamic variations of the free-space optical channel. To achieve this, the procedure detailed in Section 3 can be employed to evaluate the performance of the network over time. Unfortunately, combining the dynamics of each different unique combination of end node couples into a single figure is not straightforward. Therefore, we select three combinations of end nodes, expressing different length regimes, and evaluate their performance with minute accuracy. Here, we also evaluate different satellite constellations of up to 30 satellites in a synchronous polar orbit. The results, presented

in Figure 6, uncover the complex interplay between end-node distances and connection choices given: the satellite availability (set to 25); the end-to-end fidelity (heavily influenced by the stray light); and the weather conditions. The end-to-end fidelity is calculated taking into account spectral, temporal, and spatial filters available at the ground stations. The spectral and temporal filters are designed based on the ARC rate,  $R = 10$  GHz, so the stray light radiance is spectrally filtered accordingly, and the CAR, calculated following Equation (9), uses a detection window inversely proportional to the rate. The spatial filter performance is calculated based on a  $50 \mu\text{rad}$  field of view (FOV), typical for modern satellite and ground station telescopes, and is strongly dependent on the achievable pointing accuracy. As the results of Figure 7 demonstrate, improving the pointing accuracy and further filtering the signal spatially has a two-pronged effect: although it reduces the amount of photonic qubits that are coupled into the ground stations, it also significantly reduces the effect of stray light and is an important step towards enabling day-time operation. For the results described here, the maximum count rate of the detector is assumed to be in the GHz regime (a parameter achievable in the long-term scenario), and an FOV of  $50 \mu\text{rad}$  is chosen.

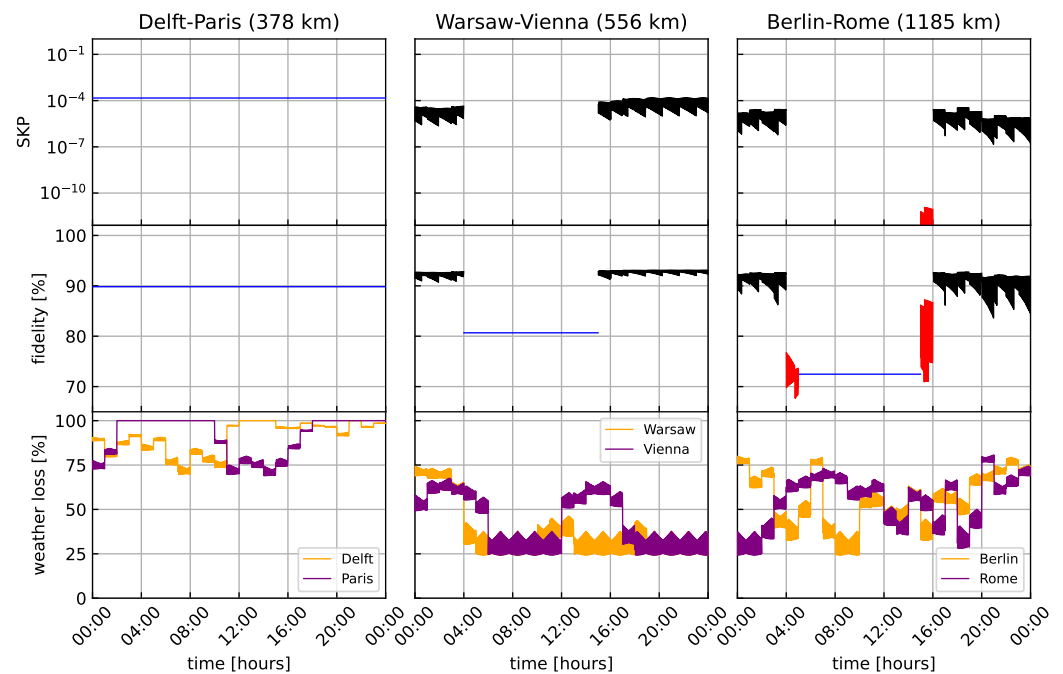


**Figure 6.** Relevant dynamic parameters with minute accuracy for 3 different combinations of end nodes: secret key generation probability (SKP), BSM fidelity, and weather-induced loss. The connection choices at each time window inherit the color-coding scheme. ARC distances are chosen to represent different regimes according to the results of Figure 6.

Clear from the figures is the fact that, over a day, the connection choices change significantly and the realistic performance cannot rely solely on the ideal case analysis of Figure 5. In particular, one could question how the value of  $d_{thres}$  changes based on the analysis over a longer time frame, such as a full day, as considered in Figure 6. Fortunately, the chosen figure of merit of key generation provides one with a quantity that can be combined: the key material extracted over a day, for instance. Combining this new performance evaluation parameter with the analysis based on  $d_{thres}$ , it is possible to analyze the proposed network for each unique end-node combination including dynamic constraints. Furthermore, the impact of a constellation of satellites can be extracted, which can then be associated to the total cost of deployment of the network’s space segment. In Figure 8, the values of  $d_{thres}$  are depicted, indicating that a similar regime switch as identified in Figure 5 (460 km) can be achieved with a number of available satellites in the range of 20.

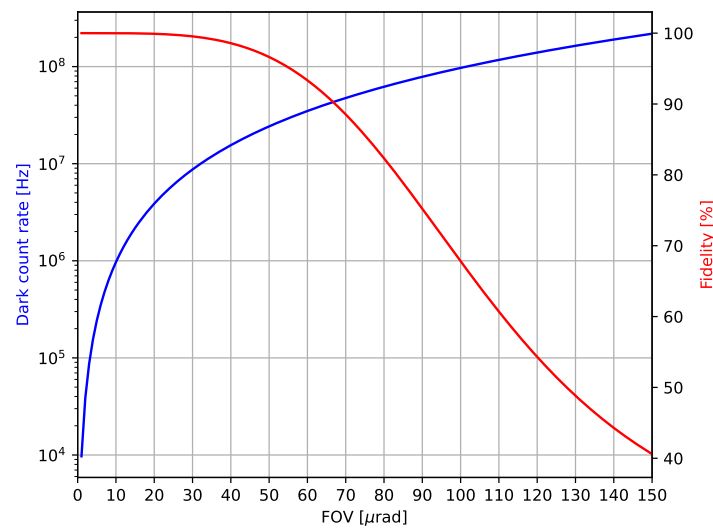


**Figure 7.** Dependency of stray-light-induced dark count rate and BSM fidelity during day-time operation (full solar radiance) for different FOVs of ground station telescope.

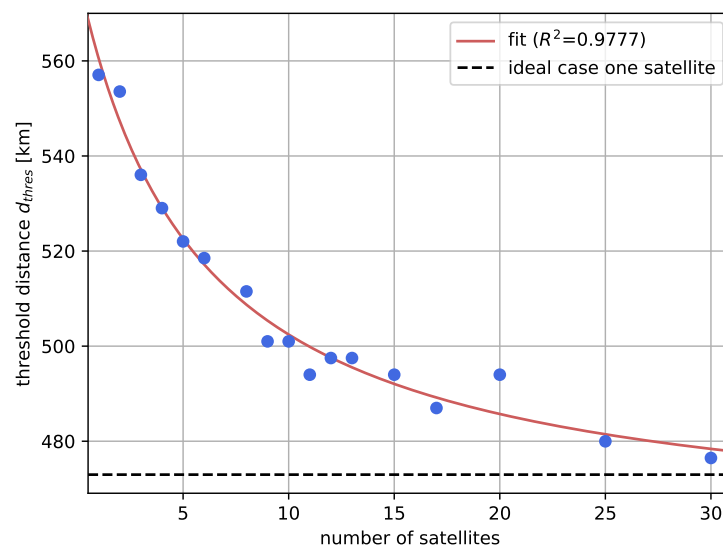


**Figure 8.** Trend of  $d_{thres}$  as a function of the number of available satellites, with the ideal case depicted as a black horizontal dotted line. The fitted curve is proportional to  $\frac{1}{x}$  and, when extrapolated, indicates that no more than 30 satellites are necessary to operate the space segment optimally.

### 5. Discussion

Architecture planning of the future quantum internet, although only expected to be implemented practically in no less than ten years, is a crucial development point. It allows for identifying physical platform candidates for sources, memories, and channels, and it also provides tools to filter through them, finding the most suitable application scenario. In particular, space-based quantum communications can benefit from this early analysis due to its intrinsic complexity and significant investment requirements and operational costs. The present analysis attempts to build upon the available literature and, through the use of specific assumptions, abstract the intricacies of the models, while maintaining rigor, to evaluate the benefits of space towards the global distribution of entanglement. The present framework distinguishes itself from similar analyses, such as [10], both when the connection between space and ground segments is allowed and in the best path estimation approach using the SKR as the figure of merit for this estimation. Furthermore, the identification of a clear regime switch for the most appropriate channel and the parameters contributing to

its threshold is a result enabled by the herewith presented framework but not the focus of the results presented in [10] or [20]. Therefore, the results of Section 4 are important since they consolidate the information contained in the models introduced in, e.g., [19,25,41], and translate it into important insight in the design of the future quantum internet.

## 6. Conclusions

Interconnecting quantum processing nodes via entanglement distribution is the task of the quantum internet which requires all the efforts available to become reality. This includes opening the door to complex forms of connectivity, such as via a space segment. In this paper, a robust analysis methodology capable of including static and dynamic constraints of the quantum channels of an ARC is proposed and used to evaluate performance estimates. A clear regime switch between ground/space segment choices is identified, and two major components (narrower spatial filtering and a satellite constellation) are highlighted as necessary to improve the overall performance. In order to interconnect nodes separated by more than 500 km, a single satellite will be able to increase the entanglement generation rates with respect to ground channels. Availability of a satellite constellation has the potential to further reduce the minimum range at which the space segment becomes beneficial. Notwithstanding, the possibility to switch connections dynamically stands out as an important feature of the future European quantum internet. For that, weather forecast and a performance prediction tool, such as the one set forth here, will be crucial for network management. Extending the analysis to include more complex space segment architectures (e.g., [46]), identifying physical platforms to implement different functional blocks (e.g., [32]), and improving the computational speed are essential points in the development of this framework left as future research directions.

**Author Contributions:** Conceptualization, G.C.A.; methodology, G.C.A., Y.J. and D.L.B.; software, D.L.B. and Y.J.; validation, D.L.B. and G.C.A.; writing—original draft preparation, G.C.A.; writing—review and editing, G.C.A., Y.J., B.P.F.D. and D.L.B.; project administration, B.P.F.D.; funding acquisition, G.C.A. and B.P.F.D. All authors have read and agreed to the published version of the manuscript.

**Funding:** This study was conducted under a Samenwerkings Middelens Onderzoek (SMO) research grant.

**Data Availability Statement:** Publicly available datasets were analyzed in this study. They can be found here: <https://www.open-meteo.com> (accessed on 17 January 2024) [44]. Simulation results can be made available upon reasonable request from the corresponding author.

**Acknowledgments:** G.C.A. and D.L.B. acknowledge fruitful discussions with F. Silvestri on free-space optical link modeling and R. Saathof on atmospheric turbulence analysis.

**Conflicts of Interest:** The authors declare no conflicts of interest.

## Abbreviations

The following abbreviations are used in this manuscript:

QIP	Quantum Information Processing
FSPL	Free-Space Path Loss
BSM	Bell State Measurement
ARC	Automated Repeater Chain
EL	Elementary Link
SNR	Signal-to-Noise Ratio
SKR	Secret Key Rate
EPR	Einstein, Podolsky, and Rosen
CAR	Coincidence-to-Accidental Ratio
QBER	Quantum Bit Error Rate
SKP	Secret Key Probability
API	Application Programming Interface
FOV	Field of View

## References

1. Wehner, S.; Elkouss, D.; Hanson, R. Quantum internet: A vision for the road ahead. *Science* **2018**, *362*, eaam9288. [[CrossRef](#)]
2. Kimble, H.J. The quantum internet. *Nature* **2008**, *453*, 1023–1030. [[CrossRef](#)]
3. Bell, J.S. On the einstein podolsky rosen paradox. *Phys. Phys. Fiz.* **1964**, *1*, 195. [[CrossRef](#)]
4. Aspect, A.; Grangier, P.; Roger, G. Experimental tests of realistic local theories via Bell's theorem. *Phys. Rev. Lett.* **1981**, *47*, 460. [[CrossRef](#)]
5. Pompili, M.; Hermans, S.L.; Baier, S.; Beukers, H.K.; Humphreys, P.C.; Schouten, R.N.; Vermeulen, R.F.; Tiggelman, M.J.; dos Santos Martins, L.; Dirkse, B.; et al. Realization of a multinode quantum network of remote solid-state qubits. *Science* **2021**, *372*, 259–264. [[CrossRef](#)] [[PubMed](#)]
6. Lago-Rivera, D.; Grandi, S.; Rakonjac, J.V.; Seri, A.; de Riedmatten, H. Telecom-heralded entanglement between multimode solid-state quantum memories. *Nature* **2021**, *594*, 37–40. [[CrossRef](#)] [[PubMed](#)]
7. Yu, Y.; Ma, F.; Luo, X.Y.; Jing, B.; Sun, P.F.; Fang, R.Z.; Yang, C.W.; Liu, H.; Zheng, M.Y.; Xie, X.P.; et al. Entanglement of two quantum memories via fibres over dozens of kilometres. *Nature* **2020**, *578*, 240–245. [[CrossRef](#)]
8. Briegel, H.J.; Dür, W.; Cirac, J.I.; Zoller, P. Quantum repeaters: The role of imperfect local operations in quantum communication. *Phys. Rev. Lett.* **1998**, *81*, 5932. [[CrossRef](#)]
9. Duan, L.M.; Lukin, M.D.; Cirac, J.I.; Zoller, P. Long-distance quantum communication with atomic ensembles and linear optics. *Nature* **2001**, *414*, 413–418. [[CrossRef](#)] [[PubMed](#)]
10. Liorni, C.; Kampermann, H.; Bruß, D. Quantum repeaters in space. *New J. Phys.* **2021**, *23*, 053021. [[CrossRef](#)]
11. Valivarthi, R.; Puigibert, M.I.G.; Zhou, Q.; Aguilar, G.H.; Verma, V.B.; Marsili, F.; Shaw, M.D.; Nam, S.W.; Oblak, D.; Tittel, W. Quantum teleportation across a metropolitan fibre network. *Nat. Photonics* **2016**, *10*, 676–680. [[CrossRef](#)]
12. Liu, J.L.; Luo, X.Y.; Yu, Y.; Wang, C.Y.; Wang, B.; Hu, Y.; Li, J.; Zheng, M.Y.; Yao, B.; Yan, Z.; et al. A multinode quantum network over a metropolitan area. *arXiv* **2023**, arXiv:2309.00221.
13. Lu, C.Y.; Cao, Y.; Peng, C.Z.; Pan, J.W. Micius quantum experiments in space. *Rev. Mod. Phys.* **2022**, *94*, 035001. [[CrossRef](#)]
14. Villar, A.; Lohrmann, A.; Bai, X.; Vergoossen, T.; Bedington, R.; Perumangatt, C.; Lim, H.Y.; Islam, T.; Reezwana, A.; Tang, Z.; et al. Entanglement demonstration on board a nano-satellite. *Optica* **2020**, *7*, 734–737. [[CrossRef](#)]
15. Zhou, Y.; Malik, P.; Fertig, F.; Bock, M.; Bauer, T.; van Leent, T.; Zhang, W.; Becher, C.; Weinfurter, H. Long-lived quantum memory enabling atom-photon entanglement over 101 km telecom fiber. *arXiv* **2023**, arXiv:2308.08892.
16. Yang, J.; Jiang, Z.; Benthin, F.; Hanel, J.; Fandrich, T.; Joos, R.; Bauer, S.; Kolatschek, S.; Hreibi, A.; Rugeramigabo, E.P.; et al. High-rate intercity quantum key distribution with a semiconductor single-photon source. *arXiv* **2023**, arXiv:2308.15922.
17. Krutyanskiy, V.; Canteri, M.; Meraner, M.; Krčmarsky, V.; Lanyon, B. Multimode ion-photon entanglement over 101 kilometers of optical fiber. *arXiv* **2023**, arXiv:2308.08891.
18. Miller, A.V.; Pismeniuk, L.V.; Duplinsky, A.V.; Merzlinkin, V.E.; Plukchi, A.A.; Tikhonova, K.A.; Nesterov, I.S.; Sevryukov, D.O.; Levashov, S.D.; Fetisov, V.V.; et al. Vector—towards quantum key distribution with small satellites. *EPJ Quantum Technol.* **2023**, *10*, 52. [[CrossRef](#)]
19. Abasifard, M.; Cholsuk, C.; Pousa, R.G.; Kumar, A.; Zand, A.; Riel, T.; Oi, D.K.; Vogl, T. The ideal wavelength for daylight free-space quantum key distribution. *arXiv* **2023**, arXiv:2303.02106.
20. Wallnöfer, J.; Hahn, F.; Gündoğan, M.; Sidhu, J.S.; Wiesner, F.; Walk, N.; Eisert, J.; Wolters, J. Simulating quantum repeater strategies for multiple satellites. *Commun. Phys.* **2022**, *5*, 169. [[CrossRef](#)]
21. Khmelev, A.V.; Duplinsky, A.V.; Bakhshaliyev, R.M.; Ivchenko, E.I.; Pismeniuk, L.V.; Mayboroda, V.F.; Nesterov, I.S.; Chernov, A.N.; Trushechkin, A.S.; Kiktenko, E.O.; et al. Eurasian-Scale Experimental Satellite-based Quantum Key Distribution with Detector Efficiency Mismatch Analysis. *arXiv* **2023**, arXiv:2310.17476.
22. Li, Z.; Xue, K.; Li, J.; Chen, L.; Li, R.; Wang, Z.; Yu, N.; Wei, D.S.; Sun, Q.; Lu, J. Entanglement-assisted quantum networks: Mechanics, enabling technologies, challenges, and research directions. *IEEE Commun. Surv. Tutor.* **2023**, *25*, 2133–2189. [[CrossRef](#)]
23. Van Milligen, E.A.; Jacobson, E.; Patil, A.; Vardoyan, G.; Towsley, D.; Guha, S. Entanglement Routing over Networks with Time Multiplexed Repeaters. *arXiv* **2023**, arXiv:2308.15028.
24. Labay-Mora, A.; da Silva, F.F.; Wehner, S. Reducing hardware requirements for entanglement distribution via joint hardware-protocol optimization. *arXiv* **2023**, arXiv:2309.11448.
25. Oliveira, R.; Oliveira, R.; Bernardes, N.K.; Chaves, R. Statistical properties and repetition rates for a quantum network with geographical distribution of nodes. *arXiv* **2023**, arXiv:2312.09130.
26. Pietx-Casas, O.; do Amaral, G.C.; Chakraborty, T.; Berrevoets, R.; Middelburg, T.; Slater, J.A.; Tittel, W. Spectrally multiplexed Hong–Ou–Mandel interference with weak coherent states. *Appl. Opt.* **2023**, *62*, 3284–3288. [[CrossRef](#)] [[PubMed](#)]
27. Askarani, M.F.; Chakraborty, K.; Do Amaral, G.C. Entanglement distribution in multi-platform buffered-router-assisted frequency-multiplexed automated repeater chains. *New J. Phys.* **2021**, *23*, 063078. [[CrossRef](#)]
28. Beukers, H.K.; Pasini, M.; Choi, H.; Englund, D.; Hanson, R.; Borregaard, J. Tutorial: Remote entanglement protocols for stationary qubits with photonic interfaces. *arXiv* **2023**, arXiv:2310.19878.
29. Bennett, C.H.; Brassard, G.; Crépeau, C.; Jozsa, R.; Peres, A.; Wootters, W.K. Teleporting an unknown quantum state via dual classical and Einstein-Podolsky-Rosen channels. *Phys. Rev. Lett.* **1993**, *70*, 1895. [[CrossRef](#)]

30. Sinclair, N.; Saglamyurek, E.; Mallahzadeh, H.; Slater, J.A.; George, M.; Ricken, R.; Hedges, M.P.; Oblak, D.; Simon, C.; Sohler, W.; et al. Spectral multiplexing for scalable quantum photonics using an atomic frequency comb quantum memory and feed-forward control. *Phys. Rev. Lett.* **2014**, *113*, 053603. [[CrossRef](#)] [[PubMed](#)]
31. Maharjan, N.; Devkota, N.; Kim, B.W. Atmospheric Effects on Satellite–Ground Free Space Uplink and Downlink Optical Transmissions. *Appl. Sci.* **2022**, *12*, 10944. [[CrossRef](#)]
32. Chen, K.C.; Dhara, P.; Heuck, M.; Lee, Y.; Dai, W.; Guha, S.; Englund, D. Zero-Added-Loss Entangled-Photon Multiplexing for Ground-and Space-Based Quantum Networks. *Phys. Rev. Appl.* **2023**, *19*, 054029. [[CrossRef](#)]
33. Lütkenhaus, N.; Calsamiglia, J.; Suominen, K.A. Bell measurements for teleportation. *Phys. Rev. A* **1999**, *59*, 3295. [[CrossRef](#)]
34. Garlington, T.; Babbitt, J.; Long, G. Analysis of free space optics as a transmission technology. *US Army Inf. Syst. Eng. Command* **2005**, *3*. Available online: <https://www.scribd.com/document/52063844/48702278-Analysis-of-Free-Space-Optics-as-a-Transmission-Technology-Mar05> (accessed on 5 March 2024).
35. Rozpędek, F.; Goodenough, K.; Ribeiro, J.; Kalb, N.; Vivoli, V.C.; Reiserer, A.; Hanson, R.; Wehner, S.; Elkouss, D. Parameter regimes for a single sequential quantum repeater. *Quantum Sci. Technol.* **2018**, *3*, 034002. [[CrossRef](#)]
36. Helsen, J.; Wehner, S. A benchmarking procedure for quantum networks. *NPJ Quantum Inf.* **2023**, *9*, 17. [[CrossRef](#)]
37. Werner, R.F. Quantum states with Einstein-Podolsky-Rosen correlations admitting a hidden-variable model. *Phys. Rev. A* **1989**, *40*, 4277. [[CrossRef](#)] [[PubMed](#)]
38. Gisin, N.; Ribordy, G.; Tittel, W.; Zbinden, H. Quantum cryptography. *Rev. Mod. Phys.* **2002**, *74*, 145. [[CrossRef](#)]
39. Klein, B.J.; Degnan, J.J. Optical antenna gain. 1: Transmitting antennas. *Appl. Opt.* **1974**, *13*, 2134–2141. [[CrossRef](#)]
40. Degnan, J.J. Millimeter accuracy satellite laser ranging: A review. *Contrib. Space Geod. Geodyn. Technol.* **1993**, *25*, 133–162.
41. Vasylyev, D.; Vogel, W.; Moll, F. Satellite-mediated quantum atmospheric links. *Phys. Rev. A* **2019**, *99*, 053830. [[CrossRef](#)]
42. Kim, I.I.; McArthur, B.; Korevaar, E.J. Comparison of laser beam propagation at 785 nm and 1550 nm in fog and haze for optical wireless communications. In Proceedings of the Optical Wireless Communications III, Boston, MA, USA, 6 February 2001; SPIE: Bellingham, WA, USA, 2001; Volume 4214, pp. 26–37.
43. Broekens, K.; Klop, W.; Moens, T.; Eschen, M.; do Amaral, G.C.; Silverstri, F.; Oosterwijk, A.; Visser, M.; Doelman, N.; Kaffa, L.; et al. Adaptive optics pre-correction demonstrator for terabit optical communication. In Proceedings of the International Conference on Space Optics—ICSO 2022, Dubrovnik, Croatia, 3–7 October 2022; SPIE: Bellingham, WA, USA, 2023; Volume 12777, pp. 758–766.
44. Free Weather API. Available online: <https://open-meteo.com/> (accessed on 17 January 2024).
45. Dijkstra, E.W. A note on two problems in connexion with graphs. In *Edsger Wybe Dijkstra: His Life, Work, and Legacy*; Association for Computing Machinery: New York, NY, USA, 2022; pp. 287–290.
46. Gündoğan, M.; Sidhu, J.S.; Henderson, V.; Mazzarella, L.; Wolters, J.; Oi, D.K.; Krutzik, M. Proposal for space-borne quantum memories for global quantum networking. *NPJ Quantum Inf.* **2021**, *7*, 128. [[CrossRef](#)]

**Disclaimer/Publisher’s Note:** The statements, opinions and data contained in all publications are solely those of the individual author(s) and contributor(s) and not of MDPI and/or the editor(s). MDPI and/or the editor(s) disclaim responsibility for any injury to people or property resulting from any ideas, methods, instructions or products referred to in the content.